sustainability

MDPI

Article

Study on the Style Design and Anchoring Mechanism of Enlarged Head Anchors

Sifeng Zhang [1], Yushuai Wang [1,*], Chao Li [1,*], Changwei Wang [2], Guojian Zhang [3] and Shengzhi Sun [4]

[1] School of Transportation Engineering, Shandong Jianzhu University, Jinan 250101, China; sddxzsf@sdjzu.edu.cn
[2] Shandong Luqiao Group Co., Ltd., Jinan 250014, China; w15610160652@163.com
[3] School of Surveying and Geo-Informatics, Shandong Jianzhu University, Jinan 250101, China
[4] Shandong Hi-Speed Constructon Management Group Co., Ltd., Jinan 250014, China; a1169915636@163.com
* Correspondence: 2021155115@stu.sdjzu.edu.cn (Y.W.); lichao21@sdjzu.edu.cn (C.L.); Tel.: +86-156-1016-0652 (Y.W.); +86-186-2517-6838 (C.L.)

Abstract: To resolve insufficient traditional bolt supports due to the complexity of geological conditions, the optimal design of an expanded head bolt was investigated by using theoretical calculations and experiments. The results show that the drawing capacity of an expanded head bolt is affected by the bearing capacity of front and rear ends, side bearing capacity, and side friction resistance. For a circular anchor bolt, stepped anchor bolt, and semi-ellipsoidal anchor bolt, with an increase in the front section's radius, the lateral friction resistance of the inner anchor section is gradually shared by the bearing force of the front end of the inner anchor section; the bearing effect of the front end of the inner anchor section is enhanced; and the pulling performance of the anchor bolt is enhanced. Therefore, the pulling force of the circular anchor bolt is at the maximum, followed by the stepped anchor bolt, and the semi-ellipsoidal bolt is at the minimum. The increase in the rear section can provide greater lateral friction resistance and end-bearing force. Compared with cylindrical enlarged head anchors, the circular, stepped, and semi-elliptic enlarged head anchors have a smaller front section but a larger rear section, and the reduction in the front section's bearing capacity is less than the increase in the side bearing capacity and rear-end bearing capacity; thus, the cylindrical bolt has the lowest pulling force. Compared with the front radius, the back radius has more influence on the drawing ability of the enlarged head anchor. The longer the inner anchorage section, the larger the distribution range in the compression zone that is formed in the soil body and the smaller the range in the tension zone that is formed in the rear. The increase in the length of the inner anchorage section is conducive to improving the reinforcement effect of the soil in front of the anchorage section in the bolt. Therefore, this parameter plays an important role in the redistribution of the soil in front of the force. The ultimate pull-out force of a circular table-shaped tensile bolt is the highest, followed by the stepped bolt, and the semi-elliptic bolt comes in third, with the cylindrical bolt exhibiting the lowest pull-out force; the circular table-shaped enlarged head anchor constitutes the best style design.

Keywords: enlarged head anchor; capacity characteristics; style design; derivation of uplift force formula

check for updates

Citation: Zhang, S.; Wang, Y.; Li, C.; Wang, C.; Zhang, G.; Sun, S. Study on the Style Design and Anchoring Mechanism of Enlarged Head Anchors. *Sustainability* **2023**, *15*, 8645. https://doi.org/10.3390/su15118645

Academic Editor: Jianjun Ma

Received: 15 April 2023
Revised: 17 May 2023
Accepted: 23 May 2023
Published: 26 May 2023

1. Introduction

In rock and soil anchorage, anchor rods have become a widely used anchoring method due to their advantages: low cost and easy installation. However, the pull-out resistance of traditional anchors (equal-diameter anchor) is limited, and it is greatly affected by the complexity of geological conditions. As a new type of anchor, the enlarged head anchor is formed by cutting and reaming the soil in the wall of the hole and filling cement slurry within a certain length range at the bottom of the anchor hole using a high-pressure jet. Compared with a common anchor, the enlarged head anchor increases the diameter of the anchor at the end of the anchoring section. This benefits the full contact between the anchor's end and the rock and soil around the anchor, effectively improving the interface's bonding force and side friction and improving the bearing capacity of the anchor to a certain extent. Additionally, due to the increase in the end's diameter, the anchor rod can better extrude the surrounding rock and soil mass in the anchoring process, and the stability of the soil–anchor system is further improved. By conducting theoretical analyses and indoor and outdoor tests, scholars have carried out research on the anchoring mechanism of this type of anchor.

Majer [1] proposed the cylindrical friction surface method in 1955, which became the earliest bolt design method. Mors [2] proposed the inverted cone method: owing to soil damage, a failed surface shape forms when the anchor plate is positioned relative to the surface of the inverted frustum of a cone shape, and its apex angle is ($90° + \varphi$), where φ is the angle of the internal friction of soil. These two methods only estimate the bearing capacity based on experience but do not carry out quantitative analyses on the specific size. Teng [3] then conducted a comparative analysis of these two methods, and the results showed that the soil inverted-cone method was more suitable for designing a deeply buried bolt, while its design error was larger for a shallowly buried bolt. Furthermore, with respect to deeply buried extension head bolts and shallow extension head bolts, many scholars believe that they should be discussed and studied separately. Choudhary [4], Mariupol'Skii [5], and Hs [6] all concluded that deeply buried and shallow anchors have different stress characteristics, and the failure surface of shallow anchors extends to the surface. An inverted cone with the bus bar as the curve is formed, while the damage to the deeply buried anchor only occurs in the soil body, and the soil near the surface is not damaged. Meyerhof [7] found that sandy soil formed due to the angle of the failure face between $\varphi/4$ and $\varphi/2$; thus, by considering φ in the calculation, the $\varphi/3$ design is more suitable. For enlarged head anchors with a relatively large diameter, the failure surface formed by the upper soil in the drawing process does not extend to the surface; thus, separating the deeply buried and shallowly buried enlarged head anchors was proposed. For expanding the bearing characteristics of the enlarged head anchor, many scholars have made theoretical predictions [8,9] and conducted laboratory tests [10], field measurements [11], and numerical simulations [12,13], finding that the enhanced bearing capacity of under-reamed anchors mainly comes from the end-bearing resistance of the "shoulders" and shear strength along the interface between soil and enlargement. Golait [14] found, by pulling enlarged head anchors, that lateral friction did not reach the peak when the end bearing capacity was at its maximum. Therefore, it is suggested that this factor should also be taken into account in the design of the ultimate bearing capacity of enlarged head anchors in practical engineering. Jeong [15] concluded that the bearing capacity of an enlarged head anchor is equal to the sum of the end-bearing force and lateral friction resistance, and under the same conditions, the lateral friction resistance of an ordinary pressure-type bolt is greater than that of an enlarged head anchor, and its end-bearing force is also lower than that of ordinary tension-type bolts. Chen [16] found that the larger the diameter of the expanded head ball, the higher the ultimate bearing capacity of the bolt, and the bearing capacity of the spherical end and the lateral friction of each segment change with the spacing of the ball. Based on this, Chen C [16] proposed the optimal design parameters for the multispherical expanded head bolt. Liao [17] found that when the lateral surface of the cylindrical enlarged head anchor increased by 0.5°–1.7° to form a cone, the bearing capacity of the enlarged head anchor improved accordingly. Murray [18] found that the ultimate uplift capacity of the enlarged head anchor should be determined by the curvature of the failure surface via the analysis of the equilibrium equation. Matsuo [19] thought that an expanded head bolt failure face has a logarithmic spiral and a tangent plane at the point on the surface of ($45° - \varphi/2$) in the process of drawing. By comparing the load–displacement curves for enlarged head anchors and ordinary bolts, Zhou [20] found that the anchoring capacity of an enlarged head anchor is better than that of ordinary bolts, and the bearing capacity of the enlarged head anchor is 1.5~2.5 times that of ordinary bolts, which is roughly the same as the conclusions drawn by Giampa [21], Wang [22], Liang [23], and Zhang [24]. Cui [25] used finite element MIDAS/GTS software (2010 version) to study the variation law of the displacement, axial force, and lateral friction of the enlarged head anchor. He observed that when the pulling force was low, the lateral friction of the enlarged head anchor played a leading role, and the load–displacement curve for the bolt presented a linear variation law. When the pulling force was large and the end-bearing force and lateral friction of the expanded head bolt acted synergistically on the soil around the end, the load–displacement curve for the bolt presented a nonlinear change law. Guo [26] applied digital photography technology and found that the deeply buried enlarged head anchor failure body formed below the soil's surface, exhibiting the shape of a closed balloon. Zeng [27] studied the mechanical mechanism of the expanded head bolt based on practical engineering and summarized the stress of the expanded head bolt into three stages: static earth pressure stage, transition stage, and plastic zone compaction–expansion stage. On this basis, he studied the factors affecting the expanded head bolt's bearing capacity. The research shows that the cohesion of soil, friction angle, and embedment depth of anchor bolts are the main factors affecting the bearing capacity of anchor bolts. Ilamparuthi [28] concluded that water content does not affect the failure mode of soil anchors. Ghaly [29] used spiral anchors with different design parameters and found that the threshold values of the depth-to-diameter ratio of the bolt also changed with respect to the sand's different compactness, and the threshold values of the dense, medium-density, and loose sand were 11, 9, and 7, respectively. Murray [18] found that surface roughness, shape, size, depth of embedment, and sand density of slabs can affect the load–displacement response in laboratory tests and proposed equilibrium and limit analysis methods for predicting the ultimate resistance.

To summarize, scholars worldwide roughly divide the research on the bearing law of enlarged head anchors into deeply and shallowly buried forms, and they introduce the concept of the depth–diameter ratio to explore the change law of the end-bearing force and lateral friction resistance of the bolt. These studies provide guiding significance for improving and expanding the ultimate bearing capacity of head bolts. However, there are few research studies on the different styles of enlarged head anchor designs at present; thus, enlarged head anchors have not been widely applied. In addition, the current design of enlarged head anchors is based more on-site construction experience or the design specification of ordinary bolts, and the design is unable to make the best use of the side friction resistance of the extended head, which produces conservative results. Therefore, it is of great theoretical guiding significance and engineering application value to study different types of enlarged head anchors.

2. Theoretical Basis and the Style Design Principle of Enlarged Head Anchors

According to different failure positions, the failure forms of anchors during pulling operations and use are mainly divided into three types: failure of the anchor body, failure of the grout–anchor contact bonding surface, and failure of the surrounding soil [30]. Therefore, the design and calculation of the anchor bolt's structure are clearly stipulated in the code based on these three features [31]. The specific formula is as follows:

① Calculation of the pull-out bearing capacity of the anchor rod reinforcement:

$$N_d \leq f_{py} \cdot A_S \tag{1}$$

$$N_d \leq f_y \cdot A_S \tag{2}$$

where N_d—design value for anchor bolt tension (N);

f_{py}—design value for the tensile strength of a steel strand or prestressed thread (N/mm^2);

f_y—design value for the tensile strength of ordinary reinforcements (N/mm^2);

A_S—cross-sectional area of the prestressed reinforcement (mm^2).

② Calculation of the pull-out bearing capacity between grout and reinforcement in the anchor section of the bolt:

$$N_d \leq f'_{ms} \cdot n \cdot \pi \cdot d \cdot L_a \cdot \xi \tag{3}$$

where N_d—design value for anchor bolt tension (kN);

f'_{ms}—design value for the bond strength between the grouting body and reinforcement body in the anchorage section (MPa);

n—diameter of the reinforcement or steel strand;

d—diameter of the steel bar or strand (mm);

L_a—length of the anchorage section (m);

ξ—when two or more steel bars or strands are used, the interface's bond strength reduction coefficient is 0.70~0.85.

③ Calculation of the pull-out capacity of the anchor under the condition of strength restriction of the surrounding soil:

$$N_d \leq \frac{f_{mg}}{K} \cdot \pi \cdot D \cdot L_a \cdot \psi \tag{4}$$

where f_{mg}—standard value for the ultimate bond strength between the grouting body and stratum in the anchorage section (MPa or kPa);

K—bond pull-out safety factor between the grouting body of the anchor rod section and stratum;

D—diameter of the drilling hole in the anchor rod's anchoring section (mm);

ψ—influence coefficient of the anchorage's length on the ultimate bond strength.

In addition, if a pressure-type or pressure-dispersion-type anchor bolt is used, the bearing area of the grouting body in the anchorage section will be checked in the design, and the calculation formula is as follows:

$$N_d \leq 1.35 \cdot A_p \cdot \left(\frac{A_m}{A_p}\right)^{0.5} \cdot \eta \cdot f_c \tag{5}$$

where N_d—design value for anchor bolt tension(N);

A_p—net contact area of a cross section between the anchor-bearing body and grouting body in the anchor section;

A_m—cross-sectional area of the grouting body in the anchorage section;

η—axial compressive strength amplification coefficient of confined grouting;

f_c—design value for the axial compressive strength of the grouting body in the anchorage section.

With the development and progress of engineering material technology, the probability of problems with respect to material strength and combination applications is greatly reduced. On the contrary, with the rapid development of society, the coverage of traffic facilities is rapidly expanding, which renders the engineering environment and geological conditions increasingly complex and construction is becoming increasingly difficult. Generally speaking, it is not necessary to consider the former of the two design requirements in the calculation of the anchor's pull-out capacity, and the calculation of the anchor's pull-out capacity under the constraint of the surrounding soil becomes the main design mode [9]. Therefore, only failure mode ③ is used to discuss the pull-out capacity of the anchor.

After completing the calculation for the rock and soil that will be reinforced and obtaining the design value for the traditional prestressed anchor force, N_d, the section of the reinforcement, anchorage length, and anchorage diameter can be determined according to the above structural design formula. Compared with the traditional anchor, the enlarged head anchor can also provide part of the "end pressure" to enhance the embedment between soil particles. Therefore, it is necessary to consider normal stress in soil reinforcements, which is caused by the end pressure of the anchorage section in the design.

3. Calculation of the Pull-Out Force of an Enlarged Head Anchor

3.1. Derivation and Calculation of the Pull-Out Force Formula

In terms of the stress form, the pull-out resistance provided by an enlarged head anchor rod mainly includes pull-out resistance T_1 provided by the side friction and pull-out resistance T_2 provided by the end bearing. The formula is as follows:

$$T = T_1 + T_2 \tag{6}$$

The calculation of T_1 and T_2 is different for variously shaped composite tension–compression anchors. Considering the simplification and economy of the current anchor construction method, this section deduces the calculation formula for the pull-out capacity of enlarged head anchors with different shapes (cylinder-shaped, frustum of a cone, stepped shape, and semi-ellipsoid).

① Cylinder-shaped:

$$V = \pi R^2{}_{cylinder} L \tag{7}$$

$$R_{cylinder} = \sqrt{\frac{V}{\pi L}} \tag{8}$$

where $R_{cylinder}$—radius of the inner anchorage section of a cylindrical, enlarged head anchor rod (m);

L—length of the inner anchorage section of an enlarged head anchor rod (m);

V—volume of the anchorage section in an enlarged head anchor bolt (m^3).

The pull-out resistance provided by side friction is denoted T_1:

$$T_1 = 2\pi R_{cylinder} L \tau_f = 2\pi R_{cylinder} L \frac{f_{mg}}{K} \psi \tag{9}$$

The pull-out resistance provided by the end bearing is denoted T_2:

$$T_2 = \pi R^2{}_{cylinder} P_D \tag{10}$$

② Frustum of a cone:

$$V = \frac{1}{3}\pi L\left(R^2{}_{frustum} + r^2 + R_{frustum} r\right) \tag{11}$$

where $R_{frustum}$—radius of the back section of the inner anchorage section of a circular enlarged head anchor rod (m);

r—radius of the back section of the inner anchorage section of a circular enlarged head anchor rod (m).

$$R_{frustum} = \sqrt{\frac{3V}{\pi L} - \frac{3r^2}{4}} - \frac{r}{2} \tag{12}$$

The pull-out resistance provided by side friction T_1:

$$T_1 = \left(\pi R_{frustum} L + \pi r L\right)\tau_f = \pi L\left(R_{frustum} + r\right)\frac{f_{mg}}{K}\psi \tag{13}$$

The pull-out resistance provided by end bearing T_2:

$$T_2 = \pi R^2{}_{frustum} P_D \tag{14}$$

③ Stepped shape:

If the stepped anchorage section is regarded as comprising several sections of cylinders with an equal length and equal distribution of the cross section's radius, the following can be obtained:

Length of a single section of the stepped anchor rod:

$$h = \frac{L}{n} \tag{15}$$

The radius of each section of the stepped anchor bolt is arranged using an equal difference that increases:

$$\begin{array}{c} r_1 = r + \frac{R_{step}-r}{n} \\ r_2 = r + 2\frac{R_{step}-r}{n} \\ r_n = r + n\frac{R_{step}-r}{n} \end{array} \tag{16}$$

The volume of the stepped anchor rod is as follows (Appendix A):

$$\begin{array}{l} V = \sum\limits_{k=1}^{n} \pi {r_k}^2 h \\ = \left[\left(\frac{R_{step}-(n-1)r}{n}\right)^2 + \left(\frac{2R_{step}+(n-1)r}{n}\right)^2 + \ldots + \left(\frac{(n-1)R_{step}-r}{n}\right)^2 + R^2{}_{step} \right] \pi \frac{L}{n} \end{array} \tag{17}$$

where R_{step}—back section radius of the inner anchorage section of a stepped enlarged head anchor rod (m);

r—front section radius of the inner anchorage section of the stepped enlarged head anchor rod (m);

n—order of the internal anchoring section of the stepped enlarged head anchor rod.

The following formula is derived:

$$R_{step} = \sqrt{\frac{6(2n+1)n^2 - 3n^2(n-1)r^2}{\pi L(n+1)(2n+1)^2}} - \frac{n-1}{2n+1} r^2 \tag{18}$$

The formula for the pulling force provided by side friction T_1 is derived:

$$T_1 = 2\pi \frac{L}{n} \left(\frac{n+1}{2} R_{step} + \frac{n-1}{2} r \right) \frac{f_{mg}}{K} \psi \tag{19}$$

The pulling force provided by the end load T_2 is as follows:

$$T_2 = \pi R_{step}^2 P_D \tag{20}$$

④ Semi-ellipsoid:

The following formula for the semi-ellipsoid surface is assumed:

$$\frac{x^2}{a^2} + \frac{y^2}{b^2} + \frac{z^2}{c^2} = 1 \text{ where } c = L, z \geq 0 \tag{21}$$

The volume formula for the semi-ellipsoid is as follows:

$$V = \frac{\frac{4}{3}\pi abc}{2} = \frac{2}{3}\pi abc \tag{22}$$

where a, b, and c are half of the length of each axis of the ellipsoid in a three-dimensional coordinate axis (m).

The formula for the pulling force provided by side friction T_1 is derived as follows:

$$T_1 = \frac{4c}{ab} \tau_f \int_0^{\frac{\pi}{2}} \sqrt{b^2 cos^2\theta + a^2 sin^2\theta d\theta} \tag{23}$$

The pulling force provided by end load T_2 is derived as follows:

$$T_2 = \pi ab P_D \tag{24}$$

3.2. Calculation and Comparison of the Pull-Out Force

Referring to specification [31], the related parameter values in the derived formula are presented in Table 1.

Table 1. Parameter values for the calculation formula.

Parameter	f_{mg}	K	ψ
Value range and value	0.10~0.15	2.0	1.3~1.6

Note: The value range for f_{mg} corresponds to the sand in the specification. The value for K is based on the corresponding value for the grade II anchorage engineering safety level. The value for ψ is related to the type of anchor bottom and the length of the anchor segment. The calculation of the following derived formula is carried out in the soil layer, and the length of the anchor segment is set within the range 4~6 m.

In addition, P_D is the resistance of the soil end at the front end of the anchor segment in the calculation formula for the pull-out force provided by the end load for each form of the anchor bolt, and its value is affected by multiple factors. To simplify the calculation, the following assumptions are made for the calculation conditions [31,32]:

(1) The embedment depth of the anchor bolt in the soil is substantial;
(2) The influence of the part above the enlarged head on the stress state of soil is very minimal and can be ignored;
(3) When pressure is applied to the soil element in a certain direction, the soil element produces lateral pressure on the plane perpendicular to this direction. Let the lateral pressure coefficient be ξ, and the magnitude of ξ is the same in all directions.

According to the literature [31,32], the calculation formula for P_D is as follows:

$$P_D = \frac{(K_0 - \xi)K_P \gamma h + 2c\sqrt{K_P}}{1 - \xi K_P} \tag{25}$$

Here, $K_0 = 1 - sin(1.3\varphi)$

$$K_P = tan^2\left(45^o + \frac{\varphi}{2}\right)$$

where φ is the internal friction angle of soil; c is soil cohesion; h is the buried depth from the center of the bolt to the ground; γ is the average soil layer weight; K_P is the passive earth pressure coefficient of soil; K_0 is the coefficient of static soil pressure; ξ is the lateral pressure coefficient, and its value ranges from 0.5 to 0.95 times K_a. K_a can be calculated as follows:

$$K_a = tan^2\left(45^o - \frac{\varphi}{2}\right) \tag{26}$$

The physical and mechanical parameters for sand are shown in Table 2.

Table 2. Physical and mechanical parameters for sand.

Soil Type	γ/kN m^{-3}	c/kPa	φ/^{o}
Sandy soil	18	0	20

From this calculation, $P_D = 116.19$ kN/m^3.

According to the parameters determined above, values are assigned to the formula derived in the above section. Table 3 shows the calculation's results, and Figure 1 shows the comparative analysis.

Table 3. Calculation results.

		Length of the Internal Anchorage Section				
		4 m	**5 m**	**6 m**	**7 m**	**8 m**
Theoretical derivation of pulling force value/kN	Cylinder-shaped	33.32513	33.44759	33.57005	33.69251	33.81497
	Frustum of a cone	55.5145	55.51451	55.51452	55.51452	55.51452
	Second-order Stepped shape	50.69843	50.86896	51.02736	51.17883	51.32597
	Third-order Stepped shape	53.83549	53.89467	53.93413	53.96231	53.98345
	Semi-ellipsoid	38.62513	38.94759	39.27005	39.27005	39.91497

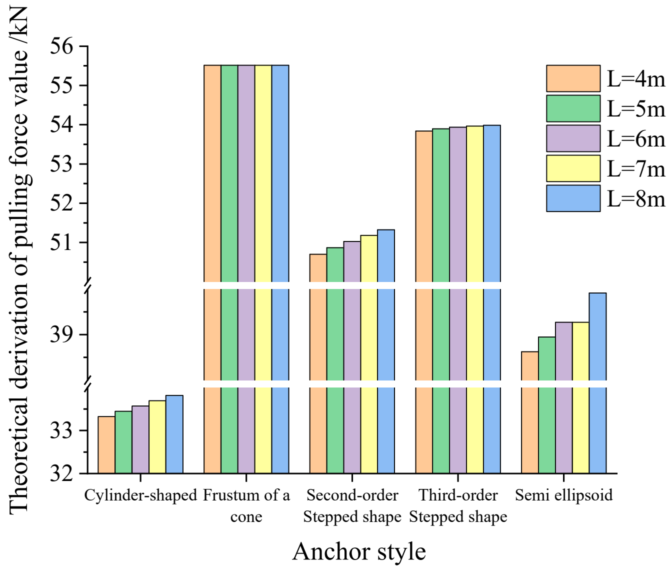

Figure 1. Histogram of the calculation values of the pull-out force of different styles of anchors.

According to Figure 1, the comparison of four types of extended head bolts shows that under the condition that the volume and length of the inner anchoring section are the same, the ultimate pulling capacity of the round-table extended head bolts is at the maximum, while that of the cylindrical extended head bolts is at the minimum. The ultimate bearing capacity of circular and cylindrical enlarged head anchors is 55.51452 kN and 33.81497 kN, respectively, for an 8 m inner anchoring section. The ultimate pulling capacity of the stepped enlarged head anchor is affected by its order and the anchoring section's length. With the increase in order n, the ultimate pulling capacity of the second and third stepped-type enlarged head anchor is 51.32597 kPa and 53.98345 kPa, respectively, when the inner anchoring section is 8 m. The ultimate pulling capacity of the semi-elliptic enlarged head anchor lies between the cylindrical and stepped enlarged head anchor. For enlarged head anchor rods, the soil around the two ends of the inner anchoring section shows compressive stress and tensile stress concentrations. The front end of the inner anchoring section is a compressive stress zone, while the tensile stress zone is mainly distributed in the soil around the rear end of the inner anchoring section. With the increase in the length of the inner anchorage section, the peak stress of the soil around the inner anchorage section gradually decreases, and the peak position shifts outward from the anchor's head. The longer the inner anchoring section, the larger the distribution range in the compression zone formed in the soil and the smaller the tension zone formed in the rear. The increase in the length of the inner anchoring section helps improve the reinforcement effect of the soil in front of the inner anchoring section of the bolt; thus, this parameter plays an important role in the redistribution of the force in front of the soil.

4. Laboratory Model Test of the Enlarged Head Anchor

4.1. Model Design

(1) Similarity ratio calculation

To better reflect the relevant conditions of the actual project, the following relevant test parameters are determined for the model test: load, P; model size, L; material unit weight, γ; elastic modulus, E; Poisson's ratio, μ; stress, σ [33,34].

The relationship of these physical quantities can be written in a general form:

$$\Sigma = f(P, L, \gamma, E, \mu) \tag{27}$$

In Formula (27), the number of physical quantities is six, and the dimensional analysis is as follows:

$$[\sigma] = f(P^a, L^b, \gamma^c, E^d, \mu^e) \tag{28}$$

In Formula (28), a, b, c, d, and e are constants that require specification, and the dimensions of the physical quantities in Formula (27) are $[\sigma] = [FL^{-2}]$, $[P] = [F]$, $[L] = [L]$, $[\gamma] = [FL^{-3}]$, $[E] = [FL^{-2}]$, and $[\mu] = [F^0L^0]$.

We substitute the above physical dimensions into Formula (28) and carry out derivations from similarity theory, and we obtain the following:

$$\pi_1 = \frac{\sigma L^2}{F},\ \pi_2 = \frac{\gamma L^3}{F},\ \pi_3 = \frac{EL^2}{F}, \pi_4 = \mu \tag{29}$$

Here, π_1, π_2, π_3, and π_4 are the similarity criteria for each physical quantity.

The size of the test model is 1:20; i.e., the geometric similarity ratio is $C_L = \frac{1}{20}$, $C_\mu = 1$, and $C_\gamma = 1$.

Subscript p is used for the original model, and subscript m is used for the reduced scale model. The values for various physical quantities obtained from this theoretical derivation are shown in Table 4.

Table 4. Values for the similarity constant of a physical quantity.

Similarity Criterion	Similarity Constant
$\pi_{1m} = \pi_{1p}$	$C_\sigma = 20$
$\pi_{2m} = \pi_{2p}$	$C_\gamma = 1$
$\pi_{3m} = \pi_{3p}$	$C_E = 20$
$\pi_{4m} = \pi_{4p}$	$C_\mu = 1$

(2) Model design and production

(1) Design and fabrication of model box soil The physical and mechanical parameters for the actual prototype soil mass are shown in Table 5. According to the calculation of the similarity ratio, $C_\sigma = 20$, $C_\gamma = 1$, $C_E = 2$, and $C_\mu = 1$. Compared with the prototype soil mass in engineering practice, the reduction parameters for the model's soil mass are C and E. Considering practical feasibility, in the process of soil preparation, the mix ratio of the model soil was restructured and adjusted many times, and soil weight, cohesion, internal friction angle, and the elastic modulus of the soil were measured. The soil preparation closest to meeting the requirements of the similarity ratio was selected, and the final ratio was determined as sand–soil–water = 1:0.18:0.95. The physical and mechanical parameters for the designed model soil mass are shown in Table 6.

Table 5. Physical and mechanical parameters for the prototype soil.

Severe γ (kN/m^3)	Cohesion C (kPa)	Angle of Internal Friction φ (°)	Poisson's Ratio μ	Modulus of Elasticity E (MPa)
18.5	20	17	0.35	42

Table 6. Physical and mechanical parameters for the prototype soil.

Severe γ (kN/m^3)	Cohesion C (kPa)	Angle of Internal Friction φ (°)	Poisson's Ratio μ	Modulus of Elasticity E (MPa)
18.5	2.2	17	0.35	5.5

(2) Design and fabrication of the model box and anchor rod

The model device comprises an external support frame, a transparent box, a cross beam, a pulley, an enlarged head anchor rod, and a loading device.

The external support frame is a rectangular parallelepiped frame with the dimensions of 930 mm × 500 mm × 600 mm (length, width, and height), and it is welded using hollow aluminum tubes with a cross section of 40 mm × 40 mm. To ensure its strength and rigidity, the four vertical side corners of the external support frame are reinforced with triangular steel plates that are 100 mm × 100 mm (two right-angle side lengths), and two vertical steel pipes are welded on the longer side of the external support frame to ensure that the maximum bending moment and shear stress of the upper steel pipe on the longer sides are at relatively lower values during the test. The size (L, W, H) of the transparent box is 650 mm × 300 mm × 500 mm. The box's body is made of transparent organic glass with a thickness of 10 mm, and the bottom is spliced by antirust steel plates with a thickness of 3 mm. The four corners of the box body are spliced by triangular steel, and they are welded and reinforced by electric welding. The external support frame and transparent box assembly are shown in Figure 2.

Figure 2. Image of the combined external support frame and transparent box device.

The beam generally comprises a hollow aluminum pipe with a cross section of 40 mm × 40 mm, and the main body is a hollow steel pipe with a length of 510 mm. The pulley is welded by multiple steel plates and plays the role of a transmitting anchor rod traction rope. After the sliding block, the loading beam and external support frame are assembled and fixed, as shown in Figure 3.

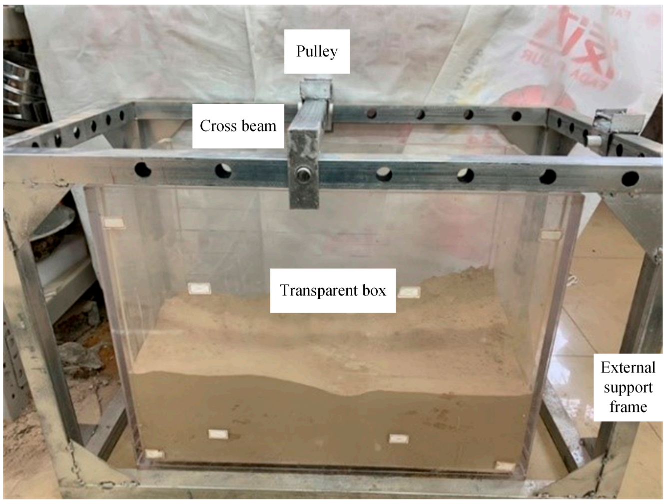

Figure 3. Fabricated sample of the assembled device.

The anchor rod body used in the model test is a steel bar with a width of 1 cm and thickness of 2 mm. The anchor rod body is placed into the self-made mold for the enlarged section, and cement mortar is poured to produce differently shaped enlarged anchor rods, as shown in Figure 4.

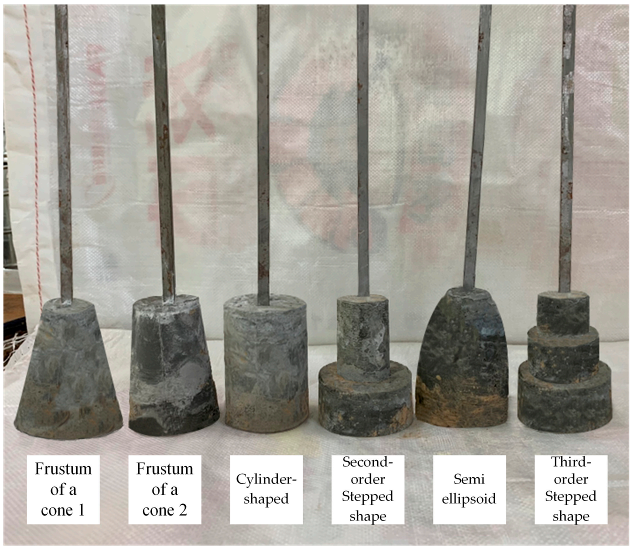

Figure 4. Different styles of enlarged head anchors.

4.2. Test Method

(1) Test soil is poured into the transparent box. When the filling height reaches a certain value, the enlarged head anchor composite is buried at the center of the transparent box, and soil continually fills the box until its height reaches a certain value; finally, the soil is leveled.

(2) One end of the traction rope is connected to the round hole at one end of the anchor rod, and it is connected with the anchor rod. The other end is connected with the weight disc, and the middle section of the traction rope is erected on the upper end and the side surface of the external support frame by virtue of the cross beam and the pulley frame. The overall diagram of the device is shown in Figure 5.

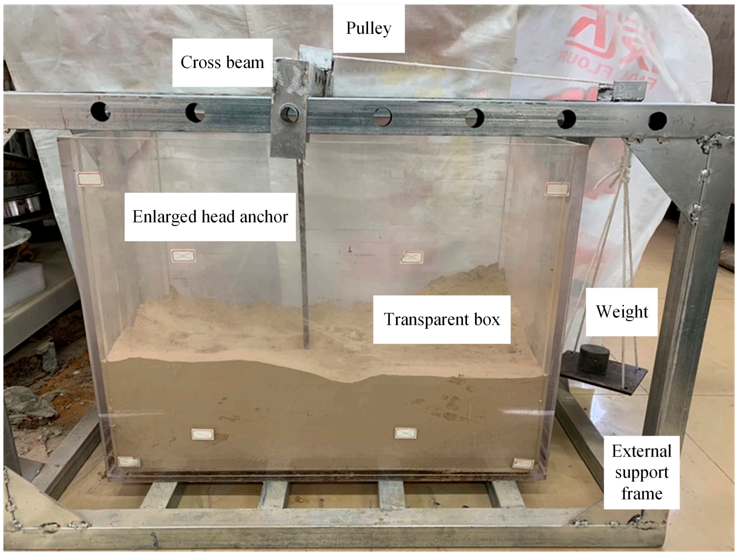

Figure 5. A large overall image of the device.

(3) According to a certain weight gradient, more weights are gradually added to the weight plate; when the anchor is pulled out uniformly, weights are no longer added. The total mass of the weight plate is obtained using a tensiometer.
(4) The anchor rod is replaced, steps 1, 2, and 3 are repeated, and the total mass value for the weight plate and weight when different anchor rods are pulled is recorded.

4.3. Results and Analysis

Table 7 shows the measured values and theoretically calculated values for the pull-out resistance of bolts with different shapes.

Table 7. Measured values and theoretically calculated values for the pull-out resistance of bolts with different shapes.

Group Number	Cylinder-Shaped	Frustum of a Cone		Stepped Shape		Semi-Ellipsoid
	1	2	3	4	5	6
Bolt size/cm	$r = R = 2.5$ $L = 10$	$r = 2.1$ $R = 2.9$ $L = 10$	$r = 1.6$ $R = 3.4$ $L = 10$	$r_1 = 1 r_2 = 3.1$ $L = 10$	$r_1 = 1 r_2 =$ $2.1 r_3 = 3.3$ $L = 10$	$a = 2.7$ $b = 3.5$ $c = 10$
Check and derive the theoretical value/N	70.809	96.382	99.386	90.461	94.461	78.037
Volume/cm^3	196.25					
Measured value for pulling force/N (g = 9.8 N/kg)	53.214 52.038 52.822 51.842	81.144 80.556 80.360 79.086	86.632 86.142 84.476 84.672	68.698 67.228 65.954 64.876	74.676 74.284 73.500 74.186	56.252 55.468 55.370 53.802

According to the measured tension values and theoretically derived values, the following diagrams are drawn. Figure 6 shows the line chart of the measured tension values for different types of enlarged head anchors. Figure 7 shows the comparison between the mean value for the measured tension and the theoretical value derived by checking calculations. In this Figure, the bar graph shows the mean value for the measured tension, and the broken line graph shows the theoretical value derived by checking calculations.

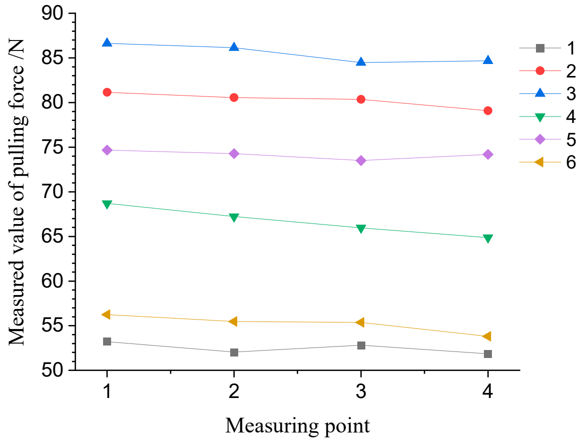

Figure 6. Line chart of the measured tension values for different types of enlarged head anchors.

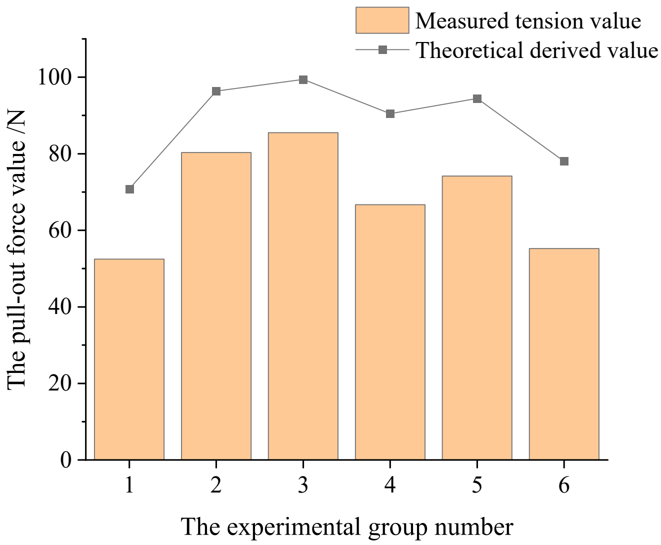

Figure 7. Comparison between the mean value for measured tension and the theoretical value derived by checking calculations.

It can be observed in Figures 6 and 7 that the measured value is similar to the theoretical value with the change in the anchor rod type. In the process of drawing, the pull-out force of the enlarged head anchor with the frustum of a cone is the largest, followed by the step-shaped anchor; the semi-ellipsoid shape ranks third, and the pull-out force of the cylinder-shaped anchor is the lowest. With the change in bolt style, the changing trend of the measured value and the theoretical value is similar, but the former is obviously smaller than the latter, and the theoretical value is about 4–5 times the measured value. The reason for this phenomenon is that the calculation condition of P_D in the derivation formula uses a burial depth of 5 m, while the burial depth of the anchor rod in the test is 1 m.

The reasons for the different pull-out resistance of different forms of enlarged head anchors are analyzed. The stress failure of enlarged head anchors is divided into three stages [35]. The first stage is the elastic stage, and the pull-out bearing capacity is mainly provided by the side friction of the common anchoring section of the anchor rod. The second stage is the elastoplastic stage. With the increase in load, the side friction resistance of the common anchoring section of the anchor reaches a peak; the anchored soil layer and the anchor are sheared; the displacement of the anchor increases; the side friction resistance of the anchor section of the enlarged head plays a role; the soil in front of the end is squeezed to increase the end resistance, and the deformation rate of the soil increases. The third stage is the development stage of the plastic zone. With the continuous increase in load, the displacement of the anchor rod increases significantly, and the soil at the front end of the enlarged head is compressed. At the same time, the stress state and the range in the plastic zone further develop, resulting in local shear failure. The enlarged head anchor rod reaches the ultimate bearing capacity.

The rear section, R, of the frustum-shaped enlarged head anchor 3 is the largest, which is 3.4 cm. With the increase in the rear section's radius, R, the side friction resistance of the inner anchoring section is gradually shared by the side's end-bearing force, and at the same time, the path of the reaction force of the soil to the inner anchoring section reaching the central axis is lengthened. In addition, the end-bearing effect at the rear of the inner anchoring section is enhanced, which improves the pull-out resistance of the anchor rod. Although the back section radius, R, of the stepped and semi-ellipsoidal enlarged head anchor is also large, the front section's radii, r, are too small at 1 cm and 0 cm, respectively, which are smaller than the front section's radii at 2.1 cm and 1.6 cm with respect to frustum-enlarged head anchors 2 and 3. With the increase in the front section radius, the side friction of the inner anchoring section is gradually shared by the end-bearing force of the front end's face, the end-bearing effect of the inner anchoring section is enhanced, and the pull-out resistance of the anchor is enhanced. Therefore, the pull-out force of the frustum anchor is the greatest, the stepped anchor comes in second, and the semi-ellipsoidal anchor exhibits the least amount of force. The pull-out resistance of the anchor rod of frustum cone 3 is greater than that of frustum cone 2 because the rear section, R, of anchor rod 3 is larger, and the front section, r, is smaller. Although the bearing capacity of the front end's face is reduced, the side and rear-end bearing capacity increase more. Compared with stepped anchor rod 4, stepped anchor rod 5 has more layers and a larger rear section, R, which can provide greater side friction and front- and rear-end-bearing forces. Compared with the cylindrical enlarged head anchor rod, the front section of the frustum, the stepped and semi-ellipsoidal enlarged head anchor rod is smaller, but the rear section is larger. The reduction in the bearing capacity of the front section is smaller than the increase in the side bearing capacity and rear bearing capacity. Therefore, the pull-out resistance of the cylindrical anchor rod is the lowest. To summarize, rear section radius R has a greater impact on the pull-out capacity of the enlarged head anchor than front section radius r.

5. Analysis of Factors Influencing the Anchoring Mechanism of an Enlarged Head Anchor

In Sections 3 and 4, it is concluded that factors such as the radius of the front and rear cross-section and the length of the inner anchorage section of the enlarged head anchor rod affect the pullout resistance of the anchor rod. To verify and further investigate the parameters affecting the pullout force of the enlarged head anchor, this section uses FLAC 3D to design the enlarged head anchor with a different radius of section after the inner anchorage section, the change rate of section before and after, and the length of the inner anchorage section, and calculates and analyzes the amount of force change in the soil and anchor rod caused by the change in different design parameters to investigate the influence law of different factors on the force condition of the anchor rod and soil, so as to conduct a systematic analysis of the anchorage mechanism of the enlarged head anchor. The influence factors on the anchorage mechanism of the enlarged head anchors are systematically analyzed.

5.1. Model Building and Parameter Selection

FLAC3D was used to build the enlarged head anchor, in which the steel strand was simulated by the anchor cable unit, and the contact surface between the grout body and the soil body was simulated by the contact interface unit. To eliminate the model boundary effect and simplify the model to reduce the computing time, the computational model was centered on the anchor body and perpendicular to the anchor plane size of a $3 \times 20 \times 3$ m soil rectangular body. The anchor rods are located in the center of the model and distributed along the long side of the model. The length of the anchorage section for both enlarged head anchor rods and conventional anchor rods is 3.0 m, and the length of free end is

14.0 m. To ensure the reliability of the comparative study of the anchorage mechanism for both types of anchor rods, the volume of anchorage section within both types of anchor rods is equal. After a preliminary trial calculation, the anchor reinforcement force at the model boundary is small and negligible, so a lateral restraint is applied around the model ($x = -3$, $x = 3$, $z = -3$, $z = 3$), and the y-directional restraint is applied on the critical surface ($y = 20$) behind the anchorage section. The 3D dimensional details of the soil model and the 3D dimensional details of the anchor are shown in Figure 8. During the simulation, the effect of self-weight stress is not considered.

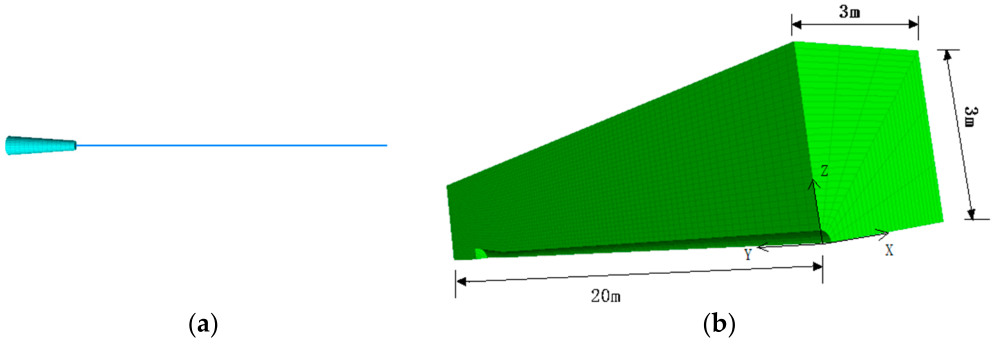

Figure 8. (**a**) Enlarged head anchor and (**b**) soil model 3D view.

The anchored section in the model adopts the linear elastic intrinsic model, and the surrounding soil adopts the Mohr–Coulomb intrinsic model, and the contact unit is set at the contact surface of both. The parameters for the soil model are consistent with Table 5. The physical and mechanical parameters related to the anchors and contact surfaces are shown in Tables 8–10 [36].

Table 8. Physical and mechanical parameters for the anchored section.

Severe γ (kN/m^3)	Poisson's Ratio μ	Modulus of Elasticity E (MPa)
25	0.2	33,500

Note: According to the protection requirements for prestressing anchor rods in specification [31], the grout in the anchorage section of prestressing anchor rods should be cement slurry or cement mortar, and its compressive strength should not be less than 30 MPa. The compressive strength of the grout in the anchorage section of pressure-dispersed anchor rods should not be less than 40 MPa, and C45 is used here. The physical and mechanical parameters are referred to specification [37].

Table 9. Material parameters for the anchor cable structural units.

Name	Anchor Cable Modulus of Elasticity (GPa)	Adhesion Strength of Anchored Section/(MPa)	Friction Angle of Anchorage Section (°)	Anchorage Section Perimeter (m)	Anchor Cable Cross-Sectional Area (mm^2)	Yield Strength of Anchor Cable (kN)
Free section	195	0	0	0.040	98	203
Anchorage section	195	0.7	38	0040	98	203

Note: The form of reinforcement refers to the specification [38], using twisted 1×7 steel wire and strength level 1720 MPa low relaxation steel strand. In the free section, the anchor cable is made of nonbonded steel strand, and the frictional force between the anchor cable and the soil is basically negligible, so the bonding strength and friction angle are taken as 0 and the interaction between the anchor cable and the slurry is stronger in the anchorage section, and the bonding strength and friction angle are taken with reference to [39].

Table 10. Contact surface parameters.

Normal Stiffness (MPa/m)	Tangential Stiffness (MPa/m)	Shear Strength (kPa)	Tensile Strength (kPa)	Friction Angle (°)	Expansion Angle (°)	Cohesion (kPa)
20	10	3.45	1.15	20.0	20.0	5

5.2. Influencing Factors and Measurement Point Arrangement

The impact factor study control group settings are shown in Table 11.

Table 11. Impact parameter values for control groups.

Simulation Group Serial Number	Radius of Section Before Inner Anchorage Section (r/m)	Radius of Section After Inner Anchorage Section (R/m)	Length ofInternal Anchorage Section Segment (L/m)	$tan\theta = \frac{R-r}{L}$	Volume of Inner Anchorage Section (V/m^3)
①	0.2	0.4	3	0.2/3	1 V
②	0.2	0.45	3	0.25/3	1.4 V
③	0.2	0.5	3	0.3/3	1.9 V
④	0.25	0.4	3	0.15/3	2.3 V
⑤	0.3	0.4	3	0.1/3	2.7 V
⑥	0.2	0.4	4	0.2/4	2 V
⑦	0.2	0.4	5	0.2/5	2.2 V
⑧	0.2	0.4	6	0.2/6	2.8 V

The schematic diagram for each parameter can be referred to Figure 9.

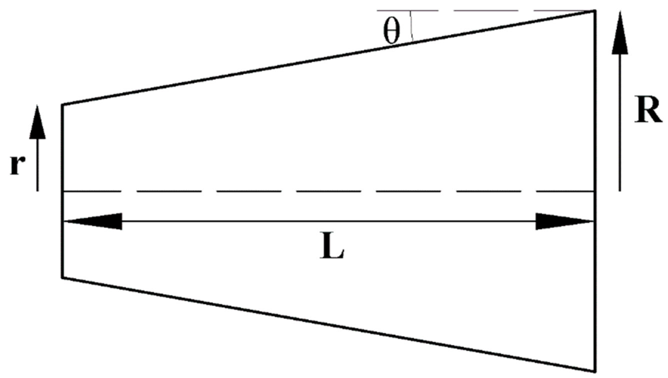

Figure 9. Schematic diagram of the dimensional parameters for the inner anchorage section.

To realize the stresses on the enlarged head anchor and soil under the influence of different factors, the measurement points are arranged according to the scheme described below. In addition, the reinforcement effect of the outer anchor head on the soil body is not considered in the monitoring and analysis process.

(1) When monitoring the anchor shaft force, the measurement points are arranged on the center axis of the inner anchorage section with the starting point coordinates (0, 14, 0) and the ending point coordinates (0, 14 + L, 0). The specific arrangement is shown in Figure 10a.

(2) When monitoring the shear stress on the outer side of the anchor, the measurement point is arranged at the outer edge of the inner anchorage section, with the coordinates

of the starting point (0, 14, r) and the coordinates of the ending point (0, 14 + L, R), as shown in Figure 10b.

(3) To monitor the soil y-directional axial force and shear force more comprehensively, the measurement points are arranged mainly along two directions. For the first direction, the monitoring starting point coordinates are (0, 5, 0.5) and the end point coordinates are (0, 15, 0.5), hereinafter referred to as the horizontal direction; for the second direction, the monitoring starting point coordinates are (0.5, 15, 3) and the end point coordinates are (0.5, 15, 0), hereinafter referred to as the vertical direction. The specific arrangement is shown in Figure 10c.

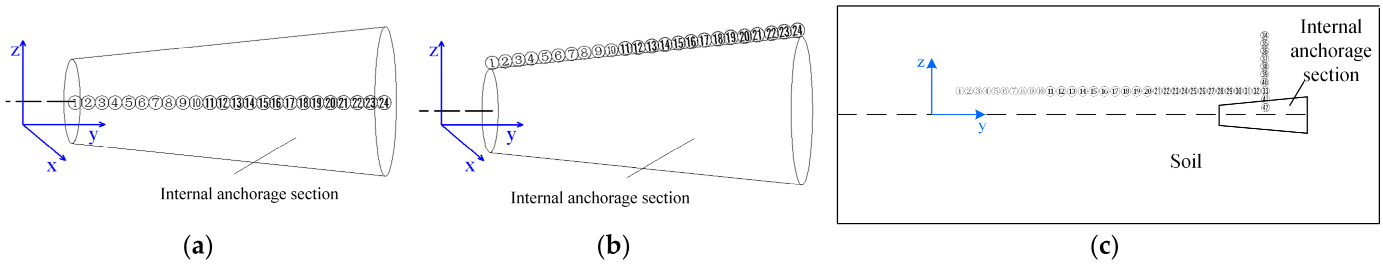

Figure 10. Diagram of the monitoring point layout location. (**a**) Anchor shaft force monitoring point layout. (**b**) Arrangement of shear stress monitoring points on the outer side of the anchor. (**c**) Arrangement of monitoring points for soil y axial force and shear stress.

5.3. Results and Analysis

(1) Influence of inner anchorage section rear section radius R

Figures 11 and 12 show the horizontal and vertical monitoring curves for soil stress σ_y under the action of the enlarged head anchor for the radius of section R behind the inner anchorage section at 0.4, 0.45, and 0.5 m.

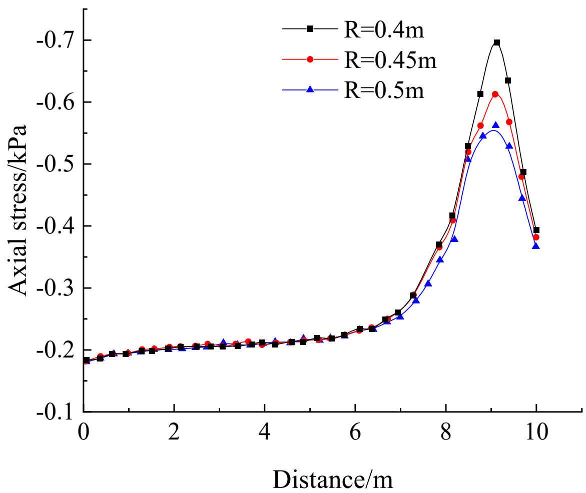

Figure 11. Soil stress σ_y distribution under the influence of section radius R after different internal anchorage sections (horizontal monitoring).

According to the two figures, soil stress σ_y around the inner anchorage section increases and then decreases along the horizontal direction from the end of the inner anchorage section to the outer anchorage head, with the peak value appearing at the front of the inner anchorage section, and gradually increases along the vertical direction from the position far from the anchor rod to the position near the anchor rod, i.e., the phenomenon of high in the middle and low in the surroundings; furthermore, with the gradual increase in radius R of the section after the inner anchorage section, stress σ_y around the anchor position generally decreases, while stress σ_y around the anchor position increases, i.e., the stress distribution spreads outward. The analysis shows that with the increase in radius R of the rear section of the inner anchorage section, the pressure value for the soil at the center is gradually shared by the side of the inner anchorage section, the stress concentration phenomenon is weakened, soil stress σ_y is spread from the anchor rod to the surrounding distribution, and the strength of the surrounding soil is more fully utilized, so the increase in radius R of the rear section of the inner anchorage section of the anchor rod improves the soil reinforcement effect.

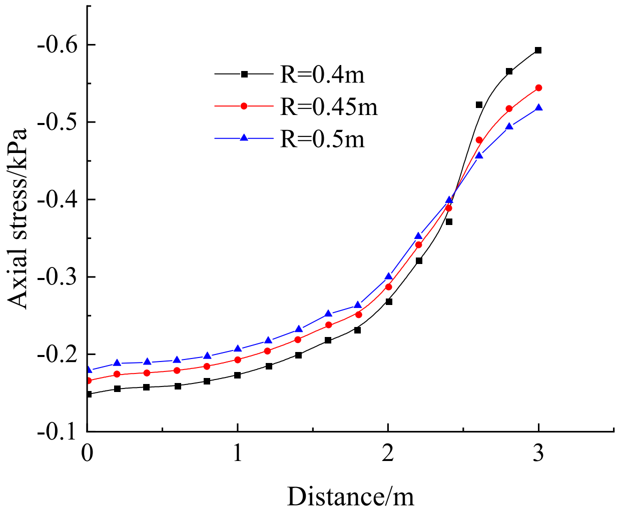

Figure 12. Soil stress σ_y distribution under the influence of section radius R after different internal anchorage sections (vertical monitoring).

Figures 13 and 14 show the horizontal and vertical monitoring curves for the soil shear stress τ under the action of the enlarged head anchor for radius R at 0.4, 0.45, and 0.5 m after the inner anchorage section.

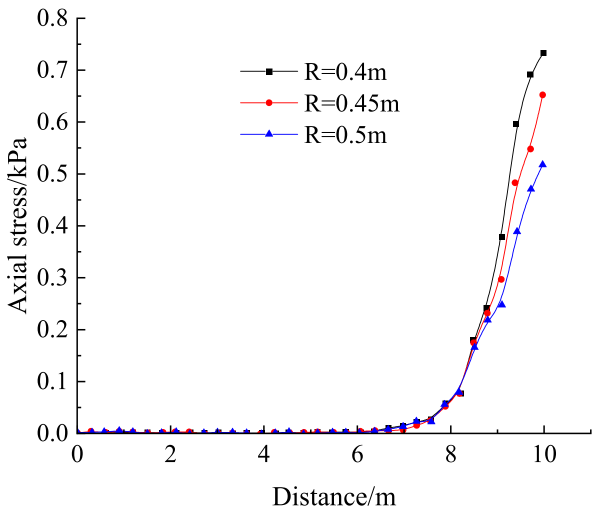

Figure 13. Soil shear stress τ distribution under the influence of section radius R after different internal anchorage sections (horizontal monitoring).

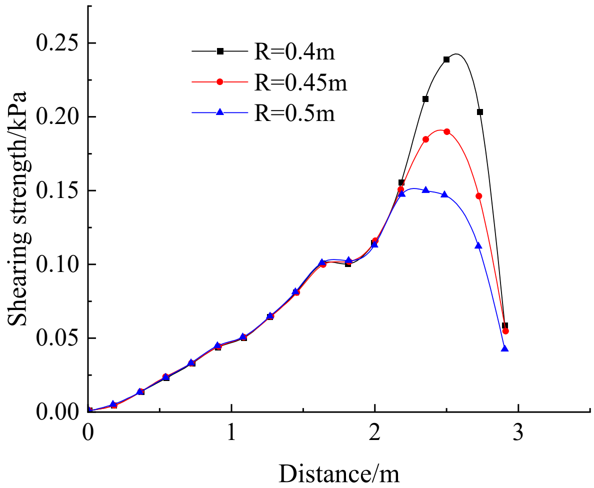

Figure 14. Soil shear stress τ distribution under the influence of section radius R after different internal anchorage sections (vertical monitoring).

According to the two figures, soil shear stress τ tends to decrease gradually along the horizontal direction from the end of the inner anchorage section to the outer anchor head, and the maximum value for shear stress appears near the middle of the inner anchorage section, and the shear stress along the vertical direction tends to increase first and then decrease from the position far from the anchor rod to the position near the anchor rod. In addition, with the increase in radius R of the section after the inner anchorage section, the peak shear stress in the vertical direction tends to shift away from the anchor rod without changing the position of the maximum value in the horizontal direction. The analysis shows that the change in radius R of the section after the inner anchorage section has little effect on the shear stress of the soil in the length direction of the inner anchorage section, and the increase in this factor has a significant effect on the soil in the vertical direction along the axis of the inner anchorage section, and its significance is mainly reflected in the decrease in the peak shear stress in the vertical direction of the axis. This conclusion is also reflected in the axial stress monitoring curve for the soil body.

Figures 15 and 16 show the monitoring curves for the axial y-direction stress level and the outer shear stress of the inner anchorage section under the action of the enlarged head anchor for radius R at 0.4, 0.45, and 0.5 m after the inner anchorage section.

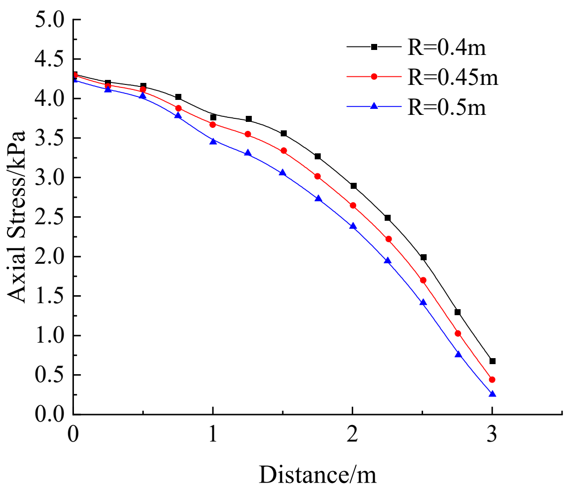

Figure 15. Axial y-direction stress diagram for the inner anchorage section under the influence of section radius R after different internal anchorage sections.

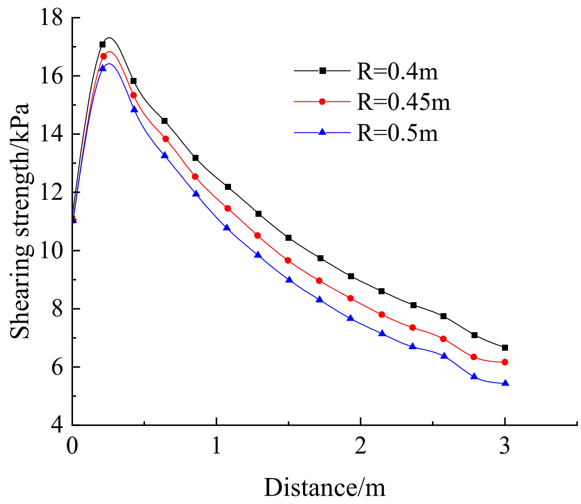

Figure 16. External shear stress diagram for the inner anchorage section under the influence of section radius R after different internal anchorage sections.

According to the analysis of the two figures, it can be seen that with the increase in radius R of the rear section of the inner anchorage section, there is a tendency to reduce the peak central tension and the peak lateral shear stress of the inner anchorage section, and the tendency of the axial tension and the lateral shear stress of the inner anchorage section decreases with the increase in the radius of the enlarged section at $1/6L$~L from the front end is more obvious, and both of them decrease with the increase in R by about 9%. The reason for this is that the increase in the radius of the rear section of the inner anchorage section, the lateral shear stress of the inner anchorage section is gradually shared by the lateral-end-bearing force, so the peak lateral shear stress and the rear shear stress decrease; furthermore, with the increase in the radius of the rear section of the inner anchorage section, the path of the reaction force of the soil on the inner anchorage section to the central axis is extended, and the rear-end-bearing effect of the inner anchorage section is enhanced, so the tensile force on the axis of the inner anchorage section decreases.

It can be seen that the increase in radius R of the rear section of the inner anchorage section of the enlarged head anchor helps to improve the status quo of the anchor-reinforcing soil with large axial tension and lateral shear force, improves the anchor reinforcement effect, and has a certain degree of positive effect in alleviating or preventing the anchor damage or the failure of the anchor–soil bond surface.

(2) Analysis of the effect of the rate of change in the anterior and posterior sections

Figures 17 and 18 show the horizontal and vertical monitoring curves for the soil's σ_y stress under the action of the enlarged head anchor with different front and rear section change rates (front section radius at 0.2, 0.25, and 0.3 m).

According to the two figures, with the decrease in the front and rear section change rate (the increase in the front section radius), stress σ_y applied to the soil gradually increases along the horizontal monitoring point, with the peak value appearing at the front end of the enlarged section, and soil stress σ_y gradually increases along the vertical direction from the far anchor end to the near anchor end. Further, unlike the effect of the change in radius R of the section after the inner anchorage section, the change in the front and rear section change rate causes soil stress σ_y to vary in the range L~$1.3L$ from the axis direction of the front end in the inner anchorage section, i.e., the change in the front and rear section change rate has a greater effect on the force on the soil in front of the front end of the inner anchorage section. The analysis shows that under the condition that the change rate of the front and rear sections decreases (the radius of front section increases), the y-directional stress value for the soil body is gradually transferred to the direction of the outer anchor head, and the soil body is subjected to more reasonable axial stress, which has a positive effect on the reinforcement effect of the soil body.

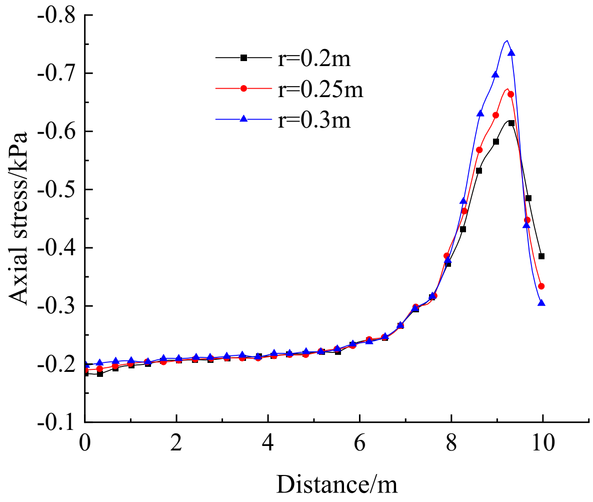

Figure 17. Soil stress σy distribution under the influence of different before and after section change rates (horizontal monitoring).

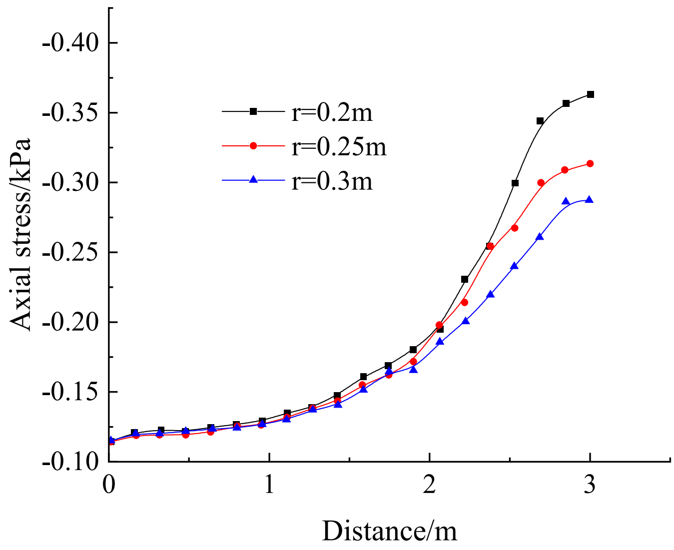

Figure 18. Soil stress σy distribution under the influence of different before and after section change rates (vertical monitoring).

Figures 19 and 20 show the horizontal and vertical monitoring curves for soil shear stress τ under the action of enlarged head anchors with different front and rear section change rates (front section radius at 0.2, 0.25, and 0.3 m).

According to the two figures, shear stress τ in the horizontal direction tends to decrease gradually from the end of the inner anchorage section to the outer anchor head, and the maximum value for shear stress appears near the middle of the inner anchorage section, and the shear stress in the vertical direction tends to increase first and then decrease from the position far from the anchor rod to the position near the anchor rod. In addition, with the decrease in the change rate of the front and rear sections (the increase in the radius of the front section), the peak shear stress of the soil tends to increase, and the peak shear stress in the front $2/3\ L$ of the inner anchorage section generally decreases without any change in the peak position in the horizontal direction, and the peak shear stress in the vertical direction does not show a tendency to shift away from the anchor rod position. The analysis shows that, unlike the effect of radius R of the rear section of the inner anchorage section, the change in the rate of change for the front and rear sections has a significant effect on the change in the reinforcement effect of the soil in the length direction of the inner anchorage section, but the decrease in this factor (the increase in the front section radius) causes an unfavorable situation of the increase in the soil shear stress in the vertical direction along the axis of the inner anchorage section of the soil.

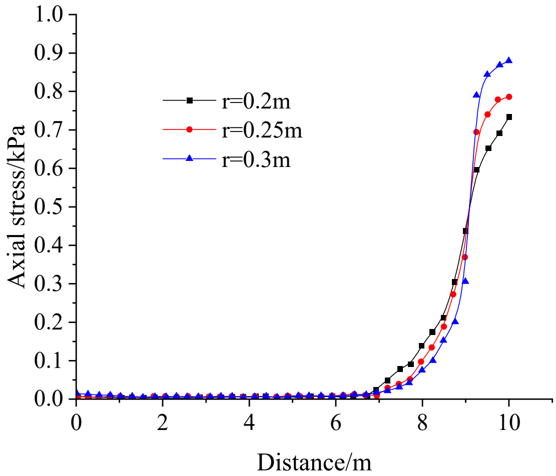

Figure 19. Soil shear stress τ distribution under the influence of different before and after section change rates (horizontal monitoring).

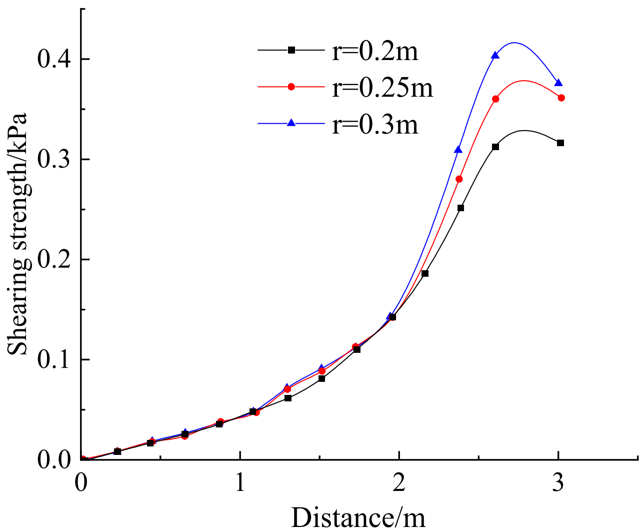

Figure 20. Soil shear stress τ distribution under the influence of different before and after section change rates (vertical monitoring).

Figures 21 and 22 show the monitoring curves for axial y-directional stress and external shear stress in the inner anchorage section under the action of tensile–compression composite anchors with different front and rear section change rates (front section radius at 0.2, 0.25, and 0.3 m).

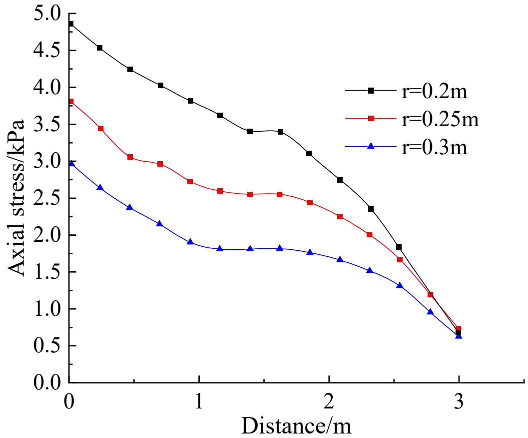

Figure 21. Axial *y*-direction stress diagram for the inner anchorage section under the influence of different before and after section change rates.

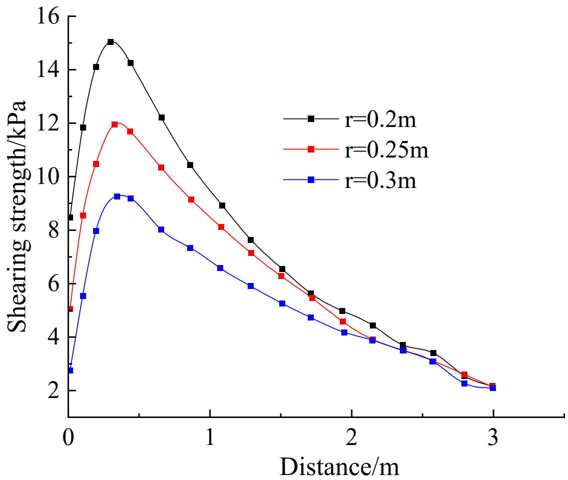

Figure 22. External shear stress diagram for the inner anchorage section under the influence of different before and after section change rates.

According to the analysis of the two figures, it can be seen that with the decrease in the front and rear section change rate (increase in the front section radius), the same effect as that of the rear section radius R of the inner anchorage section; there is a tendency to decrease the peak of the central tension and the outer shear stress of the inner anchorage section, and the tendency of the axial tension and the outer shear force of the inner anchorage section to decrease with the decrease in the front and rear section change rate at 0~5/6L from the rear of the front end is more obvious. Further, with the equal decrease in the front-to-back section variation rate, the decrease in the inner anchorage section axial tension is generally about 43% and the decrease in the outer shear force is about 16%.

The reason for this is that the decrease in the front and rear section change rate (increase in the front section radius), the lateral shear stress of the inner anchorage section is gradually shared by the front-end-bearing force, so the peak lateral shear stress and the overall shear stress decrease; furthermore, under the action of a certain pullout force, the increase in the front section radius makes the front-end-bearing effect of the inner anchorage section increase along with the reaction force of the soil on the inner anchorage section (mainly the end-bearing reaction force). The path to the central axis is prolonged, so the peak tensile value for the inner anchorage section axis and the overall tension value are reduced.

In summary, the decrease in the change rate of the cross section before and after the enlarged head (increase in the front section radius) helps to reduce the soil stress in front of the inner anchorage section and improve the reinforcement effect of the anchor rod. The effect of this parameter is more significant than the effect of the rear section radius R of the inner anchorage section for improving the current situation of the anchor rod reinforcing soil with large axial tension and external shear force.

(3) Analysis of the effect of length L of the enlarged section

Figures 23 and 24 show the horizontal and vertical monitoring curves for soil stress σ_y under the action of the enlarged head anchor for the inner anchorage section length L at 3, 4, and 5 m.

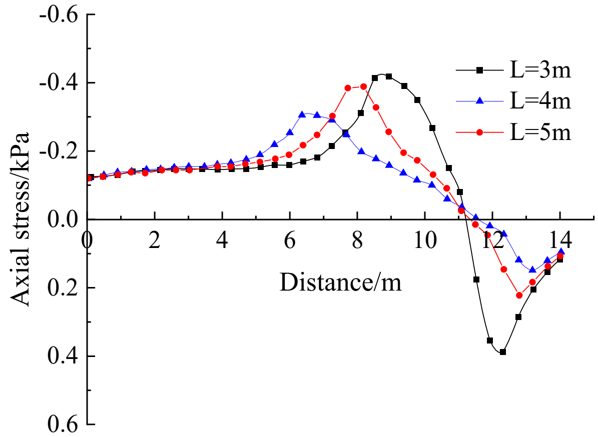

Figure 23. Soil stress σy distribution under the influence of different expanded section length L (horizontal monitoring).

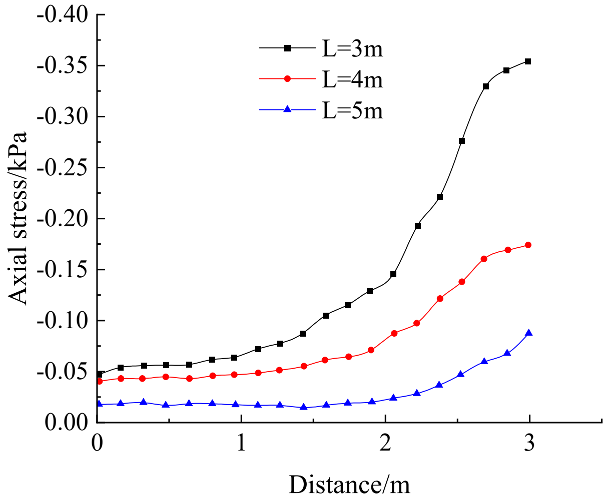

Figure 24. Soil stress σy distribution under the influence of different expanded section length L (vertical monitoring).

According to Figure 23, with the increasing length L of the inner anchorage section, the peak stress σ_y in the soil around the inner anchorage section gradually decreases, and there is a tendency for the peak position to shift toward the outer anchor head direction (the offset direction shown in the figure). Correspondingly, the longer the inner anchorage section is, the larger the distribution range in the compressive zone formed in the soil body along the horizontal direction, and the smaller the range in the tensile zone formed at the rear (the range gradually decreases, as shown in the figure), and the lower the peak maximum tensile stress. Combined with Figure 24, it can be seen that the increase in length L of the expanded section reduces the peak stress σ_y in the near-anchored soil body.

Figures 25 and 26 show the horizontal and vertical monitoring curves for the soil shear stress τ under the action of the tensile–compression composite anchor rod for length L of the inner anchorage section at 3, 4, and 5 m.

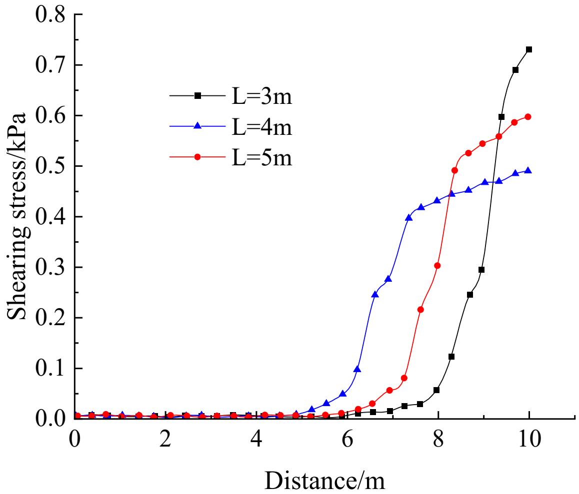

Figure 25. Soil shear stress τ distribution under the influence of different expanded section length L (horizontal monitoring).

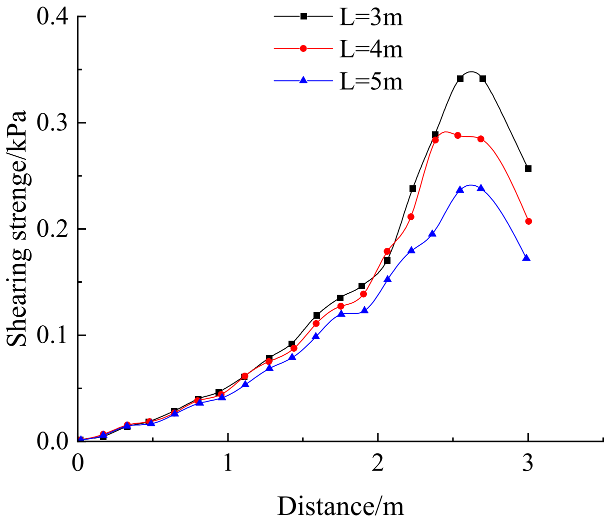

Figure 26. Soil shear stress τ distribution under the influence of different expanded section length L (vertical monitoring).

According to Figure 25, with the increase in length L of the inner anchorage section, peak shear stress τ in the horizontal direction of the surrounding soil decreases, and the distribution range in the larger shear stress in the horizontal direction tends to shift toward the outer anchor head. According to Figure 26, the peak shear stress also exists, and the distribution range does not tend to expand toward the far anchor end.

Therefore, the effect of increasing the length of the inner anchorage section L on the reinforcement of the soil in front of the inner anchorage section is more obvious than that of the surrounding soil, specifically, the increase in this parameter extends the reinforcement of the anchor toward the outer anchor head; in addition, the effect of this parameter on the reinforcement of the soil in front is more obvious than that for the rate of change in the front and rear sections, so the length of the inner anchorage section L is an important influencing factor on the redistribution of the force in front of the soil.

Figures 27 and 28 show the monitoring curves for the y-directional stress and external shear stress in the inner anchorage section under the action of tensile–compression composite anchor rod for the length of inner anchorage section at 3, 4, and 5 m.

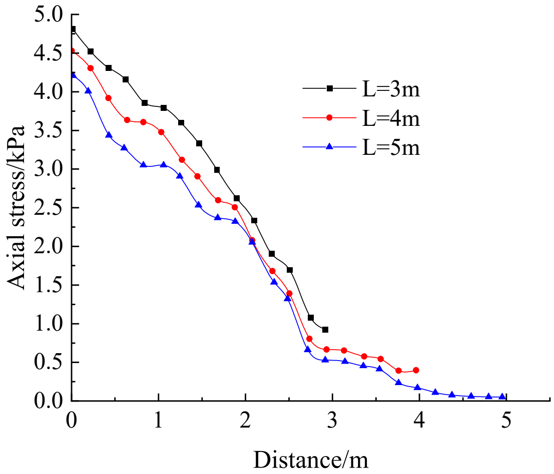

Figure 27. Axial *y*-direction stress diagram for the inner anchorage section under the influence of different expanded section length *L*.

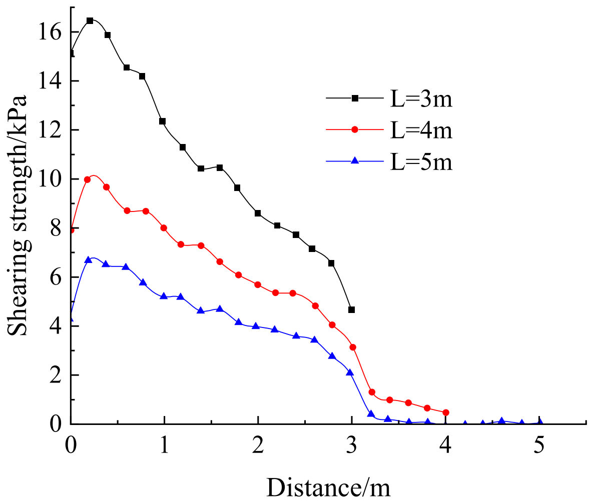

Figure 28. External shear stress diagram for the inner anchorage section under the influence of different expanded section length *L*.

According to the two figures, with the increase in the length of the inner anchorage section, the peak axial stress of the anchor rod at the front end of the inner anchorage section decreases, and the shear stress at the outside of the inner anchorage section shows a general decreasing trend along the length of the anchorage section, and even the axial force and the shear stress at the outside of the anchor rod tend to be close to zero for the range 3.5~5 m when $L = 5$ m. The reason is that, under the condition of certain pulling force, as the value for this parameter increases, the distributable range in pulling force inside the anchor rod increases, so the average value for anchor rod axial force and external shear stress decreases, while the internal force of anchor rod is gradually transferred backward along its length from the end near the outer anchor head; therefore, there is a certain critical value for the length of internal anchorage section, when its length exceeds this critical value, not only will it not share the internal stress of anchor rod, but will also cause an increase in material cost. When the length exceeds the critical value, it will not only not share the internal stress of the anchor, but also increase the material cost, which will seriously affect its economic efficiency.

6. Conclusions

In this paper, formulas for calculating the anchorage force of different types of enlarged head anchors are derived, the formulas are verified by an indoor drawing test, and the optimal scheme is selected. The conclusions follow.

(1) Under the condition that the volume and length of the extended anchorage section are the same, the ultimate pulling capacity of the cylindrical enlarged head anchor is generally less than that of the circular, stepped, and semi-elliptic enlarged head anchor, and its value is about 0.2~0.5 times the latter three. Moreover, it increases with an increase in the anchoring section's length. The ultimate uplift capacity of the circular table-shaped enlarged head anchor is obviously higher than that for the stepped, semi-elliptic and cylindrical enlarged head anchors. The ultimate uplift capacity of the circular table-shaped enlarged head anchor increases with the increase in anchorage length under the constant volume condition of the enlarged head anchor. The ultimate pulling capacity of a stepped enlarged head anchor is affected by its order and length of the anchoring section. With the increase in order n and anchoring section length L, the ultimate pulling capacity of the stepped enlarged head anchor increases. The ultimate pulling capacity of the semi-elliptic enlarged head anchor falls between the cylindrical and stepped enlarged head anchors, and its variation law is consistent with that for circular and stepped bolts. The longer the inner anchorage section, the larger the distribution range in the compression zone formed in the soil body, and the smaller the range in the tension zone formed in the rear section. The increase in the length of the inner anchoring section helps improve the reinforcement effect of the soil in front of the inner anchoring section; thus, the parameter plays an important role in the redistribution of soil that experiences the force.

(2) The drawing capacity of the expanded head anchor is affected by the bearing capacity of the front and rear ends, the side bearing capacity, and the side friction resistance. For circular anchor bolts, stepped anchor bolts, and semi-ellipsoidal anchor bolts, with the increase in front section radius r, the lateral friction resistance in the inner anchoring section is gradually shared by the bearing force of the front end of the inner anchoring section; the front-end-bearing effect of the inner anchoring section is enhanced; the bolt's pulling performance is enhanced. Therefore, the pull-out force of the circular rock bolt is the greatest, followed by that of the stepped rock bolt, and the pull-out force of the semi-elliptic rock bolt is the lowest. The increase in rear section R can provide greater lateral friction resistance and rear-end bearing capacity. Compared with cylindrical enlarged head anchors and circular, stepped, and semi-elliptic enlarged head anchors, although the front section is smaller, the rear section is larger. The bearing capacity of the front section decreases less than the side bearing capacity, and the rear bearing capacity increases; thus, the cylindrical bolt has the least pulling force. Compared with front radius r, back radius R has more influence on the drawing ability of the enlarged head anchor.

(3) The numerical calculation and analysis model of the anchor rod with expanded horizontal pullout head was established by using the numerical calculation software FLAC 3D (Version 5.0.), and the effects of the parameters such as the diameter of the rear section of the inner anchorage section, the ratio of the radius of the front and rear sections, and the length of the inner anchorage section on the soil reinforcement effect, together with the force characteristics of the anchor rod itself, were analyzed in depth, and the significance of the effects of each parameter was compared. The results showed that increasing radius R of the rear section of the inner anchorage section helped to improve the reinforcement effect of the soil perpendicular to the distribution direction of the anchor rod; decreasing the change rate in the front and rear sections and increasing length L of the inner anchorage section helped to improve the reinforcement effect of the soil in front of the inner anchorage section of the anchor rod, and the latter was better than the former.

Author Contributions: Validation, C.W.; Formal analysis, G.Z. and S.S.; Writing – original draft, S.Z., Y.W. and C.L. All authors have read and agreed to the published version of the manuscript.

Funding: This research was funded by the Natural Science Foundation of Shandong Province of China, grant number ZR2022QE082.

Informed Consent Statement: Not applicable.

Data Availability Statement: The data that support the findings of this study are available from the corresponding author upon reasonable request.

Conflicts of Interest: The authors declare no conflict of interest.

Appendix A

The formula derivation process in the manuscript is as follows:

(1) The derivation of the formula for the back section radius of the inner anchorage section of the stepped enlarged head anchor rod. The volume of the stepped anchor rod is as follows:

$$\begin{aligned} V &= \sum_{k=1}^{n} \pi {r_k}^2 h \\ &= \left[\left(\frac{R_{step}-(n-1)r}{n}\right)^2 + \left(\frac{2R_{step}+(n-1)r}{n}\right)^2 + \ldots + \left(\frac{(n-1)R_{step}-r}{n}\right)^2 + R^2{}_{step}\right]\pi\frac{L}{n} \end{aligned}$$

The following is obtained:

$$M = \left[\left(\frac{R_{step}-(n-1)r}{n}\right)^2 + \left(\frac{2R_{step}+(n-1)r}{n}\right)^2 + \ldots + \left(\frac{(n-1)R_{step}-r}{n}\right)^2 + R^2{}_{step}\right]$$

where R_{step}—back section radius of the inner anchorage section of the stepped enlarged head anchor rod(m);

r—front section radius of the inner anchorage section of the stepped enlarged head anchor rod(m);

n—order of internal anchoring section of the stepped enlarged head anchor rod.

Decomposition factor:

$$\begin{aligned} M = &\left(1^2+2^2+3^2+\ldots+n^2\right)R^2{}_{step} \\ &+2[(n-1)+2(n-2)+3(n-3)+\ldots+(n-1)(n-(n-1))]R_{step}r \\ &+\left[(n-1)^2+(n-2)^2+\ldots+2^2+1^2\right]r^2 \end{aligned}$$

Here,

$$\begin{aligned} &\left(1^2+2^2+3^2+\ldots+n^2\right) = \sum_{k=1}^{n} k^2 = \frac{n(n+1)(2n+1)}{6} \\ &2[(n-1)+2(n-2)+3(n-3)+\ldots+(n-1)(n-(n-1))] \\ &= 2-\left[n(1+2+\ldots(n-1))-\left(1^2+2^2+3^2+\ldots(n-1)^2\right)\right] \\ &= n^2(n-1)-\frac{(n-1)n(2n-1)}{3} \\ &(n-1)^2+(n-2)^2+\ldots+2^2+1^2 = \sum_{k=1}^{n-1} k^2 = \frac{n(n-1)(2n-1)}{6} \end{aligned}$$

Therefore,

$$\begin{aligned} M &= \frac{\frac{n(n+1)(2n+1)}{6}R_{step}^2+\left[n^2(n-1)-\frac{(n-1)n(2n-1)}{3}\right]R_{step}r+\frac{n(n-1)(2n-1)}{6}r^2}{n^2} \\ &= \frac{\frac{n(n+1)(2n+1)}{6}R_{step}^2+\frac{(n+1)(n-1)}{3}R_{step}r+\frac{(n-1)(2n-1)}{6}r^2}{n} \end{aligned}$$

$$V = \frac{\frac{(n+1)(2n+1)}{6}R_{step}^2+\frac{(n+1)(n-1)}{3}R_{step}r\frac{(n-1)(2n-1)}{6}r^2}{n^2}\pi L$$

By transfer, we have the following.

$$R_{step} = \sqrt{\frac{6(2n+1)n^2 - 3n^2(n-1)r^2}{\pi L(n+1)(2n+1)^2} - \frac{n-1}{2n+1}r^2} \quad \text{(A1)}$$

(2) The derivation of pulling force T_1 by the side friction of the stepped enlarged head anchor:

$$\begin{aligned} T_1 &= 2\pi \sum_{k=1}^{n} \left(R_k \tfrac{L}{n}\right)\tau_f \\ &= 2\pi \tfrac{L}{n}\tau_f \left[\tfrac{R_{step}+(n-1)r}{n} + \tfrac{2R_{step}+(n-2)r}{n} + \ldots + \tfrac{(n-1)R_{step}+r}{n} + \tfrac{nR_{step}}{n}\right] \\ &= 2\pi \tfrac{L}{n^2}\tau_f \left[(1+2+3+\ldots+n)R_{step} + (1+2+3+\ldots+(n-1))r\right] \\ &= 2\pi \tfrac{L}{n}\tau_f \left(\tfrac{n+1}{2}R_{step} + \tfrac{n-1}{2}r\right) \\ &= 2\pi \tfrac{L}{n}\left(\tfrac{n+1}{2}R_{step} + \tfrac{n-1}{2}r\right)\tfrac{f_{mg}}{K}\psi \end{aligned} \quad \text{(A2)}$$

(3) The derivation of pulling force T_1 by the side friction of the semi-ellipsoid head anchor. We obtain the following:

$$\begin{aligned} z &= z(x,y) = c\sqrt{1 - \tfrac{x^2}{a^2} - \tfrac{y^2}{b^2}} \\ T_1 &= \tau_f \iint_{\Sigma} f(x,y,z)dS \\ &= \tau_f \iint_{D_{xy}} f(x,y,z(x,y))\sqrt{1+z_x^2+z_y^2}dxdy \\ &= \tau_f \iint_{D_{xy}} cos\gamma\sqrt{1+z_x^2+z_y^2}dxdy \\ &= \tau_f \iint_{D_{xy}} \sqrt{z_x^2+z_y^2}dxdy \end{aligned}$$

Moreover,

$$\rho = sint$$

There following is then obtained:

$$0 \le t \le \frac{\pi}{2}$$

Therefore,

$$\begin{aligned} T_1 &= 4\tau_f \int_0^{\frac{\pi}{2}} d\theta \int_0^{\frac{\pi}{2}} \tfrac{csint\sqrt{b^2cos^2\theta + a^2sin^2\theta}}{abcost} costdt \\ &= \tfrac{4c}{ab}\tau_f \int_0^{\frac{\pi}{2}} \sqrt{b^2cos^2\theta + a^2sin^2\theta d\theta} \end{aligned} \quad \text{(A3)}$$

References

1. Majer, J. Zur berechnung von zugfundamenten. *Osterreichische Bauz.* **1955**, *10*, 5–6.
2. Mors, H. The behaviour of mast foundations subjected to tensile forces. *Bautechnik* **1959**, *36*, 367–378.
3. Teng, W.C. *Foundation Design*; Prentice-Hall: Hoboken, NJ, USA, 1962; Volume 1, pp. 138–139.
4. Choudhary, A.K.; Dash, S.K. Load-Carrying Mechanism of Vertical Plate Anchors in Sand. *Int. J. Geomech.* **2016**, *17*, 04016116.1–04016116.12. [CrossRef]
5. Mariupol'Skii, L.G. The bearing capacity of anchor foundations. *Soil Mech. Found. Eng.* **1965**, *2*, 26–32. [CrossRef]
6. Hsu, S.T.; Liao, H.J. Uplift behaviour of cylindrical anchors in sand. *Can. Geotech. J.* **1998**, *12*, 70–80. [CrossRef]
7. Meyerhof, G.G.; Adams, J.I. The Ultimate Uplift Capacity of Foundations. *Can. Geotech. J.* **1968**, *5*, 225–244. [CrossRef]

8. Prakash, C.; Ramakrishna, V. Lateral load capacity of underreamed piles—An analytical approach. *Soils Found.* **2008**, *44*, 51–65. [CrossRef]
9. Alekseev, A.G.; Bezvolev, S.G.; Sazonov, P.M. Experience of using multi-blade screw piles in silt-loam soil foundation. *Soil Mech. Found. Eng.* **2019**, *55*, 388–393. [CrossRef]
10. Niroumand, H.; Kassim, K.A. Uplift Response of Irregular-Shaped Anchor in Cohesionless Soil. *Arab. J. Sci. Eng.* **2014**, *39*, 3511–3524. [CrossRef]
11. Shahin, M.A.; Jaksa, M.B. Pullout capacity of small ground anchors by direct cone penetration test methods and neural networks. *Can. Geotech. J.* **2006**, *43*, 626–637. [CrossRef]
12. Rafa, S.A.; Moussai, B. Three-dimensional analyses of bored pile and barrette load tests subjected to vertical loadings. *Soil Mech. Found. Eng.* **2018**, *5*, 146–152. [CrossRef]
13. Park, H.; Lee, S.R.; Kim, N.K.; Kim, T.H. A numerical study of the pullout behavior of grout anchors underreamed by pulse discharge technology. *Comput. Geotech.* **2013**, *47*, 78–90. [CrossRef]
14. Golait, Y.S.; Padade, A.H.; Cherian, T. Prediction of Quantitative Response of Under-Reamed Anchor Piles in Soft Clay Using Laboratory Model Study. *J. Test. Eval.* **2018**, *46*, 507–522. [CrossRef]
15. Jeong, S.Y.; Choi, H.Y.; Lee, S.R. Uplift Behavior of Under-Reamed Anchors in Sandbed. *Int. J. Offshore Polar Eng.* **2007**, *17*, 317–319.
16. Chen, C.; Xia, Y.Y.; Ni, Q. Investigation on the Working Mechanism and Structural Parameters Optimization of Multiple Ball Shaped Nodular Anchors. *Soil Mech. Found. Eng.* **2020**, *57*, 49–56. [CrossRef]
17. Liao, H.J.; Hsu, S.J. Uplift Behavior of Blade-Underreamed Anchors in Silty Sand. *J. Geotech. Geoenviron. Eng.* **2003**, *6*, 129–130. [CrossRef]
18. Murray, E.J.; Geddes, J.D. Uplift of Anchor Plates in Sand. *J. Geotech. Eng.* **1987**, *113*, 202–215. [CrossRef]
19. Matsuo, M. Study on the uplift resistance of footing (II). *Soils Found.* **1968**, *8*, 18–48. [CrossRef]
20. Zhou, Z.; Zhang, L.; Han, P. Field comparative test of high pressure rotary jet enlarged head anchor. *Eng. Investig.* **2019**, *10*, 32–34. (In Chinese)
21. Giampa, J.R.; Bradshaw, A.S.; Gerkus, H.; Gilbert, R.B.; Sivakumar, V. The effect of shape on the pull-out capacity of shallow plate anchors in sand. *Geotechnique* **2019**, *69*, 355–363. [CrossRef]
22. Wang, L.; Li, J.; Wen, P. Research on bearing characteristics of enlarged head anchorage bar. *Southwest Highw.* **2016**, *3*, 49–56. (In Chinese)
23. Liang, Y. *Study on Anchoring Mechanism of Pressure Type Anchor with Reaming Hole in Soil Layer*; China Academy of Railway Sciences: Beijing, China, 2012. (In Chinese)
24. Zhang, H. Study on Mechanical Mechanism of Enlarged Head Anchor. Master's Thesis, Hebei University of Engineering, Handan, China, 2018. (In Chinese)
25. Cui, X.; He, W. Stress analysis of anchorage section of extended large anchor bolt under drawing action. *Chin. Sci. Technol. Pap.* **2013**, *8*, 381–384. (In Chinese) [CrossRef]
26. Guo, G.; Liu, Z.; Li, Y.; Yang, S.; Zhang, Y. Model experimental study on pull-out failure mechanism of expanded bolt. *Chin. J. Rock Mech. Eng.* **2013**, *32*, 1677–1684. (In Chinese)
27. Zeng, Q.; Yang, X.; Yang, Y. Mechanical mechanism and calculation method of enlarged head anchor. *Rock Soil Mech.* **2010**, *31*, 1359–1367. (In Chinese) [CrossRef]
28. Ilamparuthi, K.; Muthukrishnaiah, K. Anchors in sand bed: Delineation of rupture surface. *Ocean Eng* **1999**, *26*, 1249–1273. [CrossRef]
29. Ghaly, A.; Hanna, A.; Hanna, M. Uplift behaviour of screw anchors in sand. II: Hydrostatic and flow conditions. *Int. J. Rock Mech. Min. Sci. Geomech. Abstr.* **1991**, *28*, 794–808. [CrossRef]
30. Guo, W.; Li, C.; Gong, X.; Li, J.; Xiong, Z. Calculation and analysis of influencing factors of pullout resistance of enlarged head bolt. *Geotech. Found.* **2012**, *26*, 52–55. (In Chinese) [CrossRef]
31. *Technical Code for Geotechnical Bolt and Shotcrete Support Engineering*; China Plan Publishing House: Beijing, China, 2015. (In Chinese)
32. Li, Y.; Wang, L.; Feng, Z.; Lei, D.; Han, Y. Theoretical Analysis and Numerical Simulation of Bearing Characteristics of Anti-anchor Bolt with Enlarged Head. *Southwest Highw.* **2017**, *3*, 150–155. (In Chinese)
33. Yuan, W. *Similarity Theory and Static Model Test*; Southwest Jiaotong University Press: Chengdu, China, 1998. (In Chinese)
34. Ma, X. Experimental Study and Numerical Analysis of 3D Soil Arching in Piled Reinforced Embankments. Master's Thesis, Chang'an University, Xi'an, China, 2018. Available online: https://xueshu.baidu.com/usercenter/paper/show?paperid=1q2t00e04w2r0270hk1c0ex0u5412423&site=xueshu_se (accessed on 14 April 2023). (In Chinese)
35. Wen, P. Experimental Study on Load-Bearing Characteristics of Anchor Rod with Expanded Head. Master's Thesis, Zhengzhou University, Zhengzhou, China, 2016. Available online: https://xueshu.baidu.com/usercenter/paper/show?paperid=32de6c152c6c0dffe56a52d2cf65bf2a&site=xueshu_se&hitarticle=1 (accessed on 14 April 2023). (In Chinese)
36. Chang, S. *Handbook of Engineering Geology*; Architecture and Building Press: Beijing, China, 2013. (In Chinese)
37. *GB/T5224-2003*; Steel Strand for Pre-Stressed Concrete. Standard Press of China: Beijing, China, 2003. (In Chinese)

38. Fu, W.; Zhuo, Z.; Ren, X. Experimental study on the adhesive strength of anchor slurry and tendon in soil layer. *J. Geotech. Eng.* **2018**, *40*, 1300–1308. (In Chinese) [CrossRef]
39. Zhang, Y.; Rao, L.; Tang, S.; Xu, M.; Luo, B. Shear strength test of prestressed anchor cable grouted body and rock bonding interface. *Chin. J. Highw.* **2008**, *6*, 1–6. (In Chinese)